Deuterium implantation into Y_2O_3-doped and pure tungsten: Deuterium retention and blistering behavior

M. Zhao[a,b], W. Jacob[b,*] A. Manhard[b], L. Gao[b], M. Balden[b], U. von Toussaint[b], Z. Zhou[a]

[a] *School of Materials Science and Engineering, University of Science and Technology, Beijing, Beijing 100083, China*

[b] *Max-Planck-Institut für Plasmaphysik, Boltzmannstr. 2, Garching 85748, Germany*

Abstract: The blistering and near-surface deuterium retention of a Y_2O_3-doped tungsten (W) and two different pure W grades were studied after exposure to deuterium (D) plasma at elevated temperatures (370, 450 and 570 K). Samples were exposed to a deuterium fluence of 6×10^{24} D m^{-2} applying a moderate ion flux of about 9×10^{19} D m^{-2} s^{-1} at an ion energy of 38 eV/D. Morphological modifications at the surface were analyzed by confocal laser scanning microscopy and scanning electron microscopy. The D depth profiles and the accumulated D inventories within the topmost 8 μm were determined by nuclear reaction analysis. Blistering and deuterium retention were strongly dependent on the implantation temperature. In addition, blistering was sensitively influenced by the used tungsten grade, although the total amount of retained D measured by nuclear reaction analysis was comparable. Among the three different investigated tungsten grades, Y_2O_3-doped W exhibited the lowest degree of surface modification despite a comparable total D retention.

Keywords: Tungsten, Tungsten Alloys, Deuterium Retention, Plasma-Surface Interaction, Morphology

PACS: 28.52.Fa, 52.40.Hf, 79.20.Rf, 81.05.Ni

Published in:	Journal of Nuclear Materials **487** (2017) 75-83.
doi:	10.1016/j.jnucmat.2017.02.005
Submitted:	22.09.2016
Accepted:	02.02.2017
Available online:	06.02.2017

1. Introduction

Owing to their refractory nature and good thermal properties, tungsten (W) and tungsten alloys are considered as promising candidate materials for plasma-facing components in fusion devices such as ITER and DEMO [1,2,3]. However, these materials exhibit serious embrittlement problems at low temperatures particularly in conjunction with recrystallization and neutron irradiation [4,5,6,7]. Recently, some authors have demonstrated that fine dispersed particles (such as TiC [8,9,10,11] , Y_2O_3 [12,13,14], La_2O_3 [15,16], etc.) in the W matrix can counteract the brittleness through a decrease of the ductile-to-brittle transition temperature (DBTT) and an increase of the recrystallization temperature. In its role as a plasma-facing material (PFM), however, tungsten would be subject to high heat fluxes and huge hydrogen particle fluxes. On the one hand, hydrogen irradiation will lead to the evolution of vacancies, voids and blisters, finally resulting in the degradation of the material's physical and mechanical properties [17,18]. On the other hand, hydrogen retention in tungsten is a major safety and economic concern in fusion reactors [19]. Therefore, it is of significant importance to evaluate the surface modification and deuterium retention behavior of doped W materials with respect to their use as PFM in fusion devices.

The published experimental database on the W+H system contains evidence of a variety of blister-like structures and hydrogen retention that depend strongly not only on the plasma exposure conditions, such as impact energy, flux, fluence and sample temperature, but also on details of the tungsten microstructure [20,21], e.g., grain size and texture, impurities and defect densities (vacancies, voids and dislocations). Adding dispersion particles into W may provide additional trapping sites for hydrogen and may thus, e.g., change the blistering behavior and increase hydrogen retention. Studies of surface modification and retention in W−TiC [22,23], and W−La_2O_3 [24] have been started recently. However, so far research data for yttrium-oxide-doped tungsten (W−Y_2O_3) on this issue is still not available.

In our previous work [14,25], a highly condensed fine-grained W−Y_2O_3 alloy was fabricated from mechanically alloyed W and Y powders in collaboration with Beijing Tian−Long Tungsten & Molybdenum Co. Ltd (TLWM, China). It was reported that this W−Y_2O_3 alloy exhibited high fracture strength and obvious ductile behavior at low [25] and high temperatures [14] and good transient thermal shock resistance [14]. Therefore, the first aim of this work is to provide data belonging to a series of experiments dedicated to study the surface modification and deuterium retention of W−Y_2O_3 by exposure to suitable deuterium plasma. The second aim of this work is to study the influence of the W grade on blistering and near-surface retention by comparing W−Y_2O_3 with two different pure W grades. One of the pure W grades was provided by TLWM, having a similar production route and grain structure as the W material doped with Y_2O_3. The other one was fabricated by Plansee SE (Austria). This pure W grade has been subjected to extensive studies with detailed parameter scans [20,21,26,27,28,29].

2. Experimental details

2.1 Specimens

W doped with about 1.24 wt% Y_2O_3 ($W-Y_2O_3$) used for this study was fabricated from mechanically alloyed W (purity: 99.97 wt%) and Y (1 wt%) powders. The detailed procedure for the preparation of mechanically alloyed powders can be found in [25]. The subsequent production route for this material was developed in collaboration with TLWM. It consists of four steps [25]: (1) preliminary densification of mechanically alloyed W−Y powders to square geometry by cold isostatic pressing at a pressure of 220 MPa; (2) sintering densification in flowing hydrogen atmosphere at temperatures above 2270 K for 4 h; (3) one-way rolling for obtaining a ~5.5 mm plate with a deformation of about 75 %; (4) removal of residual stresses by a heat treatment to obtain better mechanical properties, e.g., strength and toughness.

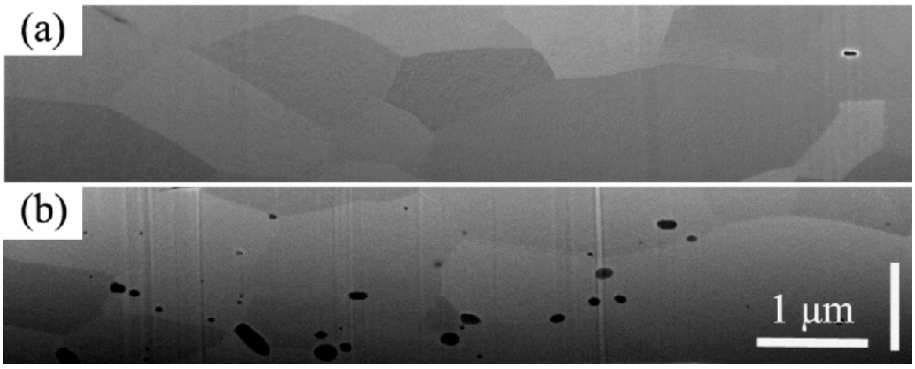

Fig. 1: *Cross-section SEM images of W−T (a) and W−Y_2O_3 (b). Shown are the cross sections perpendicular to the sample surface and perpendicular to the rolling direction prepared by FIB cutting. The two cross-sections are horizontally titled by 38° with respect to the viewing plane, resulting in compressed distances in vertical direction by a factor of 0.79 (see vertical scale bar). The scale bars are valid for both images. The grains show a similar size and grain aspect ratio (length to width). The round-shaped black areas in (b) are Y_2O_3 particles.*

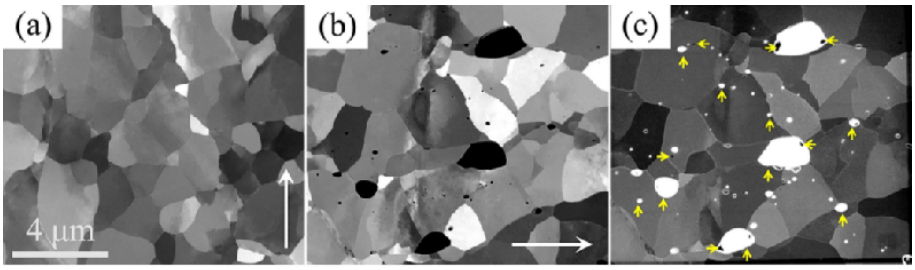

Fig. 2: *Top-view SEM images of W−T (a) and W−Y_2O_3 (b and c). The long white arrows indicate the rolling direction. The scale bar is valid for all images. (a) and (b) were acquired with a concentric backscattered electron detector (CBS), while (c) representing the same area as (b) was captured using a secondary electron detector (SE). The two materials have a similar grain size distribution. Y_2O_3 particles – identified by EDX – are marked by vertical yellow arrows in (c) and residual pores by horizontal yellow arrows.*

The two investigated pure W grades provided by different manufactures (Plansee SE, Austria and TLWM, China, respectively) were used for comparison. The pure W from Plansee SE has a guaranteed purity of 99.97 wt% while the pure W from TLWM has a nominal purity above 99.95 wt%. More than 20 different kinds of impurity elements are listed in the chemical composition table of the pure W grades. The Plansee SE material was delivered after rolling to a ~1.5 mm thick plate and subsequent grinding to 0.8 mm, the detailed fabrication process is confidential. The TLWM pure W was rolled in a fabrication process similar to that for

W−Y_2O_3 to a ~7 mm plate, corresponding to a deformation rate of 75 %. To distinguish these two pure W specimens, they will be termed as W−P (P = Plansee SE) and W−T (T = TLWM) throughout this paper.

The rolling process leads to variations in the grain morphology (size and shape) and in preferred grain orientation, depending on the degree of deformation [30,31]. Differences in the grain morphology and grain orientation might influence the blistering behavior of the specific tungsten material [20,28]. In general, after rolling, the grains are elongated along the rolling direction. For W−P the (sub-) grain dimension perpendicular to the plate surface is the smallest with 0.5~1 μm, while parallel to the plate surface the typical size is 1−5 μm [32,33]. The grain structure of W−T and W−Y_2O_3 is shown in Figs. 1 and 2. Both materials have a similar grain structure. The typical grain size parallel to the specimen surface is 1−5 μm, while perpendicular to the specimen surface the size is 0.4−1.6 μm. That means, W−T and W−Y_2O_3 have smaller grain aspect ratio (length to width) than W−P. This is due to the lower degree of deformation of the former two. In Figs. 1(b) and 2(b), many small black dots can be seen. In the latter figure, large black grains are also visible. Fig. 2(c) shows the surface microstructure of the same area as Fig. 2(b), but in different imaging mode. Fig. 2(b) was acquired with a concentric backscattered electron detector (CBS) while Fig. 2(c) was captured using a secondary electron detector (SE). CBS mode is sensitive to the compositional contrast but also to grain orientation contrast. Energy-dispersive X-ray spectroscopy (EDX) analysis indicates that the black dots and the large black grains visible in CBS mode are Y_2O_3 particles. In addition to the information from the backscattered electrons, the secondary electrons give rise to a rather good topographic contrast. Note that because of charging the Y_2O_3 particles that look black in CBS mode appear white in SE mode, while pores still appear black in SE mode because secondary electron emission from pores is suppressed. It further has to be noted that the surface of Y_2O_3 particles is always recessed compared with the surfaces of surrounding W grain (see Fig. 3). This is due to a higher etching rate of Y_2O_3 particles during chemical etching which is the final step during sample polishing (see Sect. 2.2). Because of the edge effect in SE mode the white Y_2O_3 particles appear larger than they are in reality. The true size of the Y_2O_3 particles is visible in CBS mode. A careful comparison of the big black grains in Fig. 2(b) with the corresponding white grains in Fig. 2(c) reveals that the latter are all larger. In this regard, the residual pores visible in Fig. 2 are most probably not located inside Y_2O_3 particles as it appears in Fig. 2(c), but at grain boundaries. A Transmission Electron Microscopy (TEM) image showing the exact position of residual pores in the investigated W−Y_2O_3 alloy is available in literature [25]. The residual pores visible in this TEM image are located between W grains and Y_2O_3 particles, i.e., at the W/Y_2O_3 interface. As for the distribution of Y_2O_3 particles, the small ones are mainly inside W grains while the large ones are distributed along W grain boundaries (Fig. 2), which is consistent with the report in [25].

All of these W materials contain intrinsic unavoidable impurities such as carbon (C) and oxygen (O). For the two pure W grades these impurity concentrations are very small (below 30 wt ppm). However, due to the contamination with grinding media and/or the leakage of atmosphere during ball milling process W−Y_2O_3 has small traces of extra impurities (in weight ppm), such as Mo around 300 (≈ 0.058 at.%), C around 280 (≈ 0.43 at.%) and O around 2500 (≈ 2.90 at.%) [25]. In comparison to the intrinsic C and O impurities of the

investigated pure W specimen, the amount of C in W−Y_2O_3 increased by an order of magnitude, and more significantly, the amount of O increased by two orders of magnitude. In this respect, it should be noted that the majority of the O in W−Y_2O_3 has reacted with Y to form the high-temperature-stable Y_2O_3 particles and most of the C has reacted to WC [25].

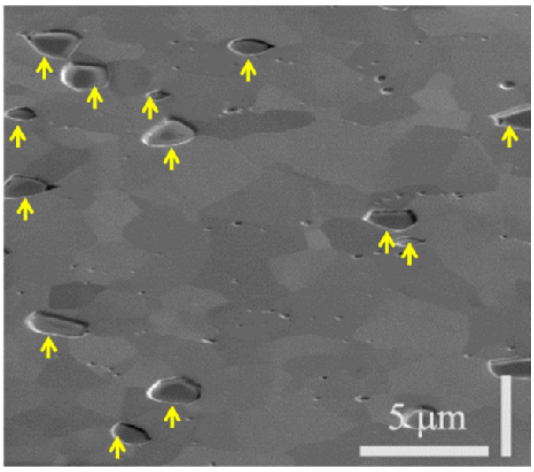

Fig. 3: *SEM image of W−Y_2O_3 after chemo-mechanical polishing and ultrasonic cleaning. The surface is horizontally tilted by 52°. The distance in vertical direction is compressed by a factor of 0.62. Y_2O_3 particles are marked by yellow arrows. They were identified by EDX analysis.*

2.2 Specimen preparation and plasma exposure

Prior to implantation, samples were cut by electric discharge machining (EDM) to 10×10×0.8 mm^3. The exposed surface is parallel to the plate surface, i.e., parallel to the rolling direction. The residue from the cutting process was removed by coarse grinding of the sample with SiC sand paper. As described in [33], the specimens were then polished to mirror finish with a final polishing step involving chemical etching to remove the distorted surface layer due to the previous mechanical polishing steps. After polishing and ultrasonic cleaning the specimens were degassed in a high-vacuum furnace at a pressure of 10^{-4} Pa and a temperature of 1200 K for 2 h. This temperature is high enough to remove any polishing residue from the surface, as well as some impurities, vacancies and dislocations in the near surface layer without leading to recrystallization or grain growth.

All of the different specimen types were exposed simultaneously to deuterium plasma using the well-quantified plasma device PlaQ [34]. For the used exposure conditions, i.e., 1.0 Pa D_2 gas pressure, the impinging ion flux is composed of 94 % D_3^+ ions, 3 % D_2^+ ions and 3 % D^+ ions. Details of PlaQ can be found in [34]. All of the samples were irradiated to a fixed fluence of 6×10^{24} D m^{-2}. The incident D flux was fixed at ~9×10^{19} D m^{-2} s^{-1} and the ion energy at 115 eV. This ion energy corresponds to an energy of 38 eV/D for the dominant ion species (D_3^+). The implantation temperatures investigated here were 370, 450 and 570 K. For 370 and 450 K, an open circuit thermostat with silicon oil was used to stabilize the sample holder temperature. For higher temperatures, e.g., 570 K the sample holder was radiation heated by a BORALECTRIC® heater element. The sample holder temperature was measured independently by a thermocouple that is pressed against the sample holder from below. Additionally the temperature of the plasma-facing surface was directly measured by a

microbolometer infrared camera.

2.3 Nuclear reaction analysis (NRA)

The D amount and the depth profile in the near surface region were measured by ion beam analysis using the D (^{3}He, p) ^{4}He nuclear reaction at different ^{3}He energies varied from 0.5 to 4.5 MeV. The cross section of this nuclear reaction peaks at ~620 keV ^{3}He energy [35]. The depth, which is probed for D, depends on the primary energy since the ^{3}He ions lose energy as they penetrate the target. The applied experimental conditions yield a maximum information depth of about 8 μm. The produced high energy protons from NRA were counted using a thick, large-angle solid state detector at a scattering angle of 135° equipped with a parabolic slit reducing the solid angle to 29.9 msr. The protons from the nuclear reaction at different ^{3}He energies were evaluated to obtain the underlying depth profile using NRADC which is a sophisticated analysis program applying Bayesian statistics [36]. These NRA measurements were carried out 4~7 days after deuterium implantation. The total accumulated D inventory was calculated from the integration of the depth profile. It represents an average value over the analyzing spot which has an area of 1 mm^2. More details on the experimental set-up for the nuclear reaction analysis (NRA), the depth resolution and the data evaluation can be found in [21,36,37].

2.4 Surface morphology

The surface morphology of the samples before and after D exposure was investigated by a confocal laser scanning microscopy (CLSM, Olympus LEXT OSL 4000) and scanning electron microscopy (SEM, HELIOS NanoLab 600, FEI and XL30 ESEM, FEI). The height and lateral dimensions of the surface modifications were determined by CLSM. The size and shape of the grains in the surfaces and in the cross sections were analyzed by SEM, which is sensitive to small variations in the grain orientation (crystal orientation contrast). That means the sub-grains separated by low-angle and high-angle boundaries are detected and their size and shape are determined [32]. Furthermore, the exposed surfaces were examined by energy dispersive X-ray spectroscopy (EDX). In order to compare the grain structure perpendicular to the rolling direction, cross sections were obtained by focused ion beam (FIB) cutting after coating the surface in situ with a Pt-C-layer. The FIB and coating system are included in the HELIOS device. For SEM imaging of the cross sections, there is an angle of 38° between the normal of the cross section plane and electron beam.

3. Experimental results

3.1 Surface modification

Fig. 4 shows surface morphologies of various W specimens after deuterium plasma exposure at 370, 450, and 570 K. Specimen surfaces prior to D plasma exposure are essentially identical to those after exposure at 570 K. The sub-figures are arranged such that the same material appears in the columns and the same exposure temperature in the rows. This figure clearly demonstrates the strong influence of implantation temperature and specimen type on the surface modifications after exposure to D plasma. For all three different types of W specimen the general trend is similar although the details of the surface features differ significantly. Before we start with the detailed discussion of the experimental results we

would like to add the following statement: Different surface features significantly depend on the experimental parameters as well as the deformation mechanisms [20]. However, so far an accurate and unambiguous naming system for these surface features after D exposure has not been developed. Therefore, in this work all of the surface features due to the exposure to D plasma will be termed as “blisters”.

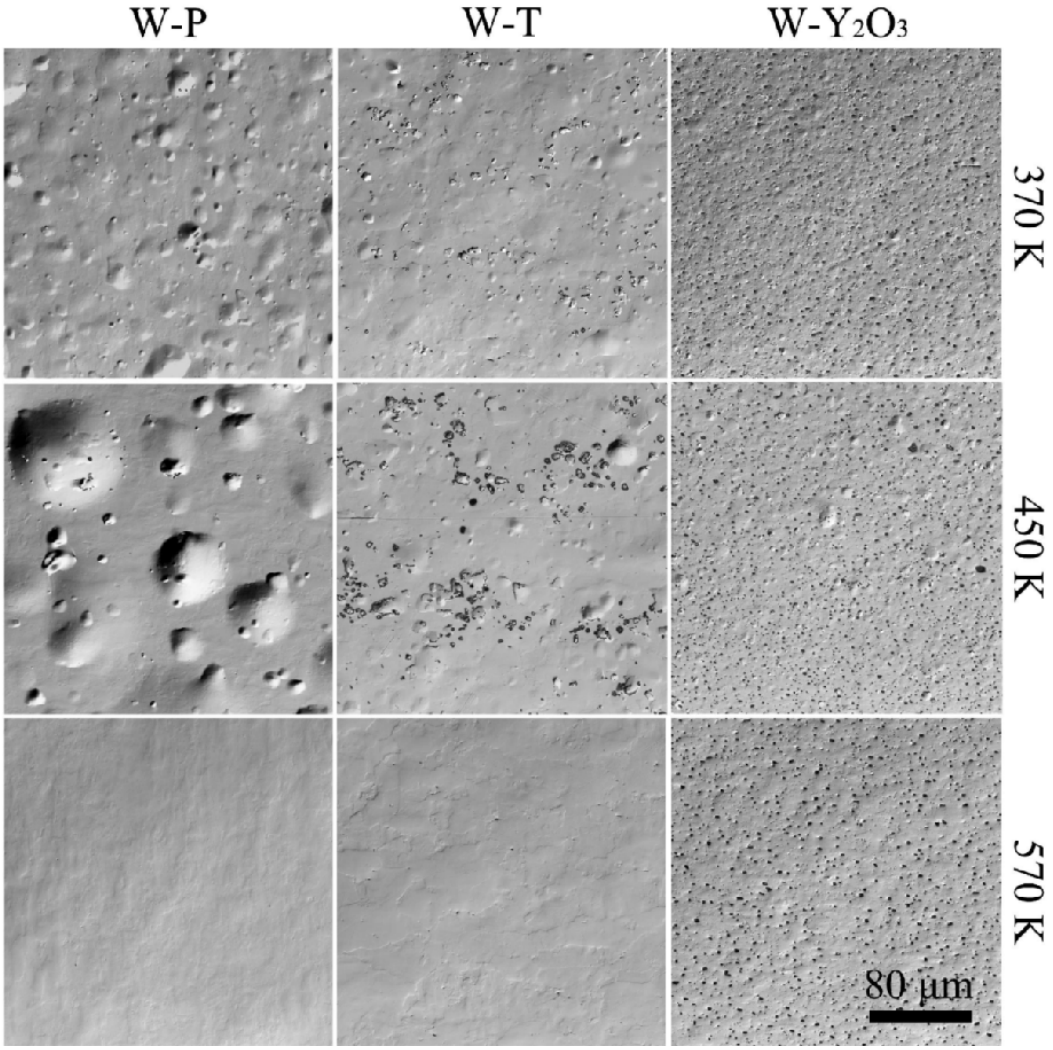

Fig. 4: *CLSM images of exposed surfaces of various tungsten materials after D plasma exposure at different temperatures. The scale bar is valid for all images. The black areas visible in the images of W−Y_2O_3 are Y_2O_3 particles. They are uniformly distributed in the W matrix. The residual pores cannot be seen in these images of low magnification. Specimen surfaces prior to D plasma exposure are essentially identical to those after exposure at 570 K.*

After exposure at 370 K the surfaces are covered with a large number of small blisters. After exposure at 450 K the blister density is somewhat lower, but the blisters are in average larger and higher than those at 370 K. After exposure at 570 K no blister was detected on any of the samples. On the surface of W−P, most blisters have an almost spherical shape and their mean size is larger than those for the other two materials. The mean blister size for W−P is larger than the mean grain size. It has been shown previously by M. Balden et al. [20] that for W−P the blisters extend across several grains. They are filled with a high pressure of D_2 gas [29]. Qualitatively the trend observed here for the size and density of blisters on W-P is in

agreement with previous investigations of the same material under similar conditions (see, e.g., [21]). For W−T, although some of the blisters had domed shapes similar to W−P, most of the blisters are smaller and had complex plateau−like shapes. For the same exposure condition, the blisters on the surface of W−Y_2O_3 are much smaller than those on W−T. Particularly after exposure at 370 K the blisters are hardly visible in Fig. 4. But on the SEM image with a higher magnification (Fig. 5), the blisters on the surface of W−Y_2O_3 exposed at 370 K are clearly discernible. They have diameters up to a few hundred nanometers and appear only inside individual W grains.

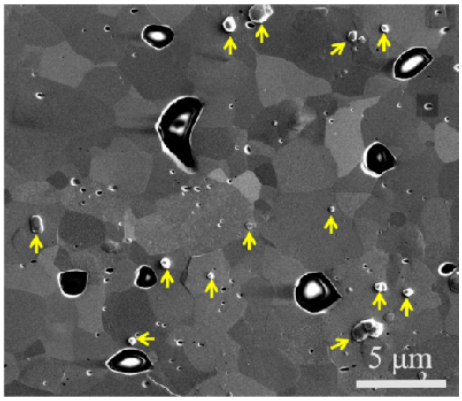

Fig. 5: *SEM image of the surface of W−Y_2O_3 exposed at 370 K. The black areas are Y_2O_3 particles. Some of the large Y_2O_3 particles appear white in the center because of charging. The edges caused by the different etching rate between W and Y_2O_3 particles also show white color. The blisters inside individual W grains are marked by yellow arrows.*

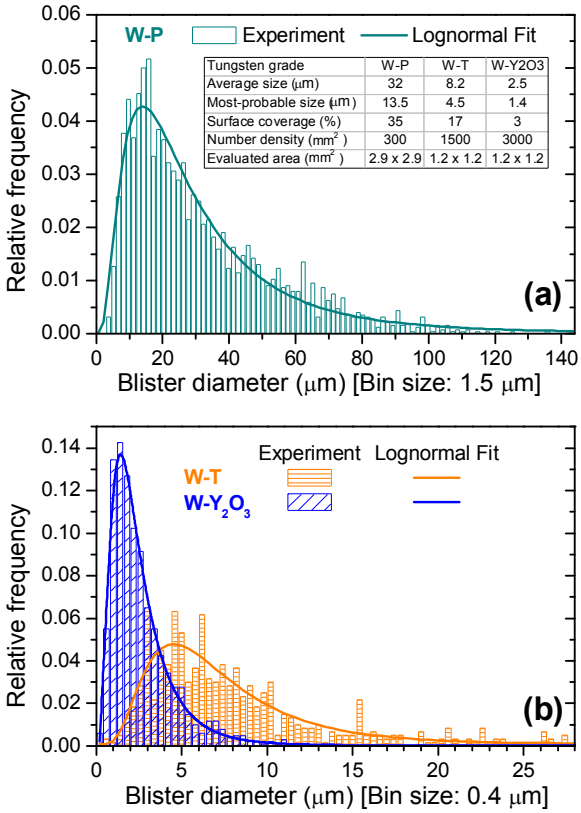

Fig. 6: *Blister size distribution compiled from CLSM images for various tungsten materials exposed at 450 K, shown as a function of equivalent blister diameter. The solid lines indicate fits with log-normal distributions.*

In order to provide a quantitative assessment on how blister diameter varies with the type of W specimen, we present lateral size distributions of blisters (Fig. 6) and three dimensional (3 D) CLSM images showing the height of blisters for each W specimen (Fig. 7). Because blisters on the surface of the W specimens exposed at 450 K are best distinguishable, we make a detailed comparison for the three W materials exposed at 450 K only. The histograms of the determined blister size distributions are depicted in Fig. 6. In each case, individual blisters were identified from the CLSM images and binned according to their equivalent diameter (i.e., the diameter of a circle with same projected area.). The equivalent diameter was obtained by manually marking the lateral extension of the blister with a straight line. Blisters that touch each other are counted as separate blisters and small blisters on top of large blisters (this occurs often for W−P) are not counted. Furthermore, distinguishing blisters from surface roughness was difficult below 80 nm, and hence, no blisters smaller than 80 nm were evaluated. The surface coverage with blisters was estimated assuming circular shapes with the determined equivalent diameters. Each of the three shown blister size distributions can be well described with a log-normal distribution. The solid lines in Fig. 6 show the fitted log-normal distributions. Such distributions arise in many materials processes, where time-dependent nucleation and growth kinetics are important [38,39]. Fig. 7 shows the 3 D CLSM images of various W specimen types, corresponding to the 2 D CLSM images for 450 K in Fig. 4. For better visibility, the values in z direction are enlarged by a factor of 20 in Fig. 7.

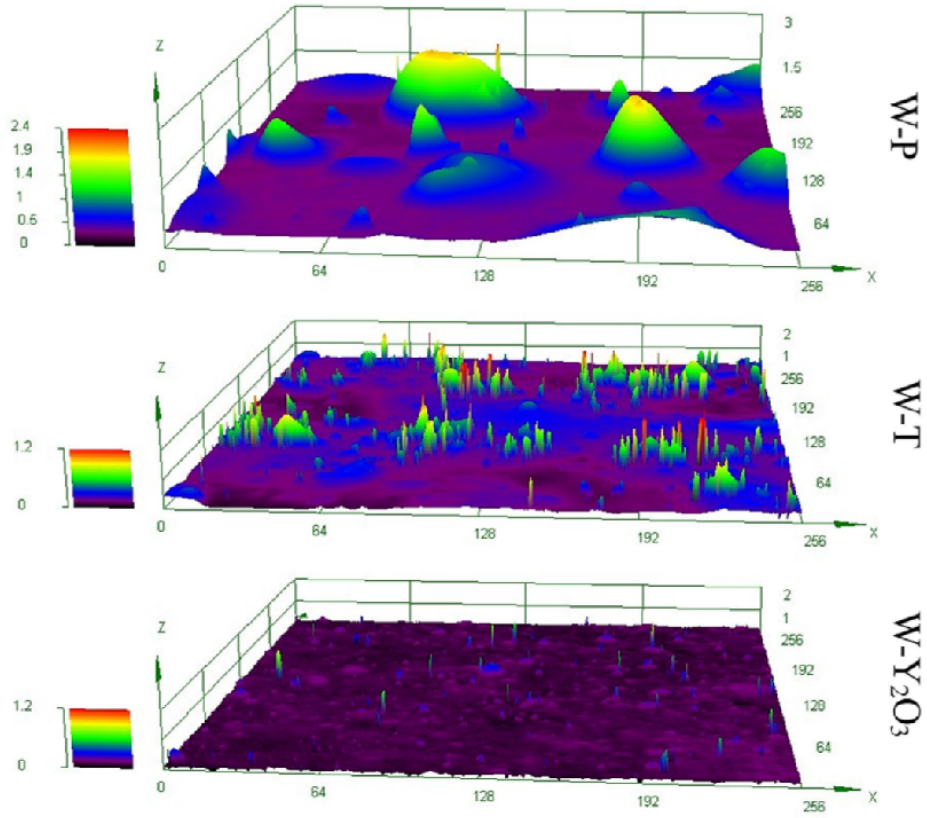

Fig. 7: *3 D CLSM images of various tungsten materials exposed at 450 K showing the height of blisters (in µm). The corresponding 2 D CLSM images were shown in Fig. 4. The values in z direction were increased by a factor of 20 for all images. The z-scale for W−P is a factor 2 higher than for the other materials.*

After exposure at 450 K, W−P shows spherical blisters with an average blister diameter of 32 μm (see Fig. 6). Frequently, small blisters are found on top of the larger blisters (Fig. 4). For blisters in the size range of 3−30 μm their height is below 0.7 μm, while for larger ones (>30 μm), it is 1.1−2.0 μm (Fig. 7). These blisters cover about 35 % of the total surface area of W−P with a number density of 300 blisters/mm^2. The quantitative values for blister size and number density differ somewhat from those reported in [21], but are of the same order of magnitude. The differences can probably be attributed to small differences in the experimental conditions, since the blistering behavior indeed reacts very sensitively to, e.g., temperature variations [21]. The blisters on the surface of W−T appear often in groups with plateau−like shapes (Fig. 4) and lower height (0.1−1.2 μm, Fig. 7). The blister diameter of this specimen varies from 0.5 μm up to 30 μm. The average blister diameter is 8.2 μm, which is only a quarter of the blister size of W−P. Surprisingly the number density is about a factor of 5 higher than that on W−P. On W−T, the blisters occupy about 17 % of the total surface area. In contrast to the appearance of grouped blister on W−T, the blisters on W−Y_2O_3 tend to appear separated and uniformly distributed (Figs. 4 and 7), and the sizes of the blisters seem to be in average smaller (average diameter: 2.6 μm, height range: 0.2−0.8 μm). Due to the fact that the blister size on W−Y_2O_3 is close to the lower limit of the detectable size range of the CLSM, the actual maximum of the lateral size distribution would shift to lower blister size if a substantial fraction of the blisters actually remained undetected in this analysis. Even though the blisters on W−Y_2O_3 show a number density of 3000 blisters/mm^2, which is a factor of two higher than on W−T, they cover less than 3 % of the total surface area on W−Y_2O_3.

3.2 Deuterium retention analysis

Fig. 8a shows the D depth profiles in the topmost 8 μm determined by NRADC [36] from the NRA data (see Sect. 2.3) for the different investigated W materials. Fig. 8b presents the accumulated D inventories as a function of depth. The accumulated D inventories were calculated from the D depth profiles (Fig. 8a) by integration of the D amount from the surface to the given depth. Both figures clearly show that the D retention behavior significantly depends on the implantation temperature, while it is only slightly influenced by the W grade.

All D depth profiles exhibit a surface peak with a D concentration of the order of 1 to 4 %. The thickness of this D-rich surface layer is for the used experimental condition set to 25 nm. This thickness is determined by the achievable depth resolution of the NRA measurement parameters and details of the NRADC data evaluation. Recent investigations by Gao et al. [40] have shown that the real thickness of this D-rich layer is smaller than 25 nm and consequently the local D concentration in the D-rich near surface layer is higher. However, for the following comparison of D retention in the here investigated three W grades the details of the D concentration profile within this very thin surface layer are not relevant. For all investigated temperatures, the surface D concentration maximum of W−Y_2O_3 shows a comparable value as for the two pure W grades (see Fig. 8a).

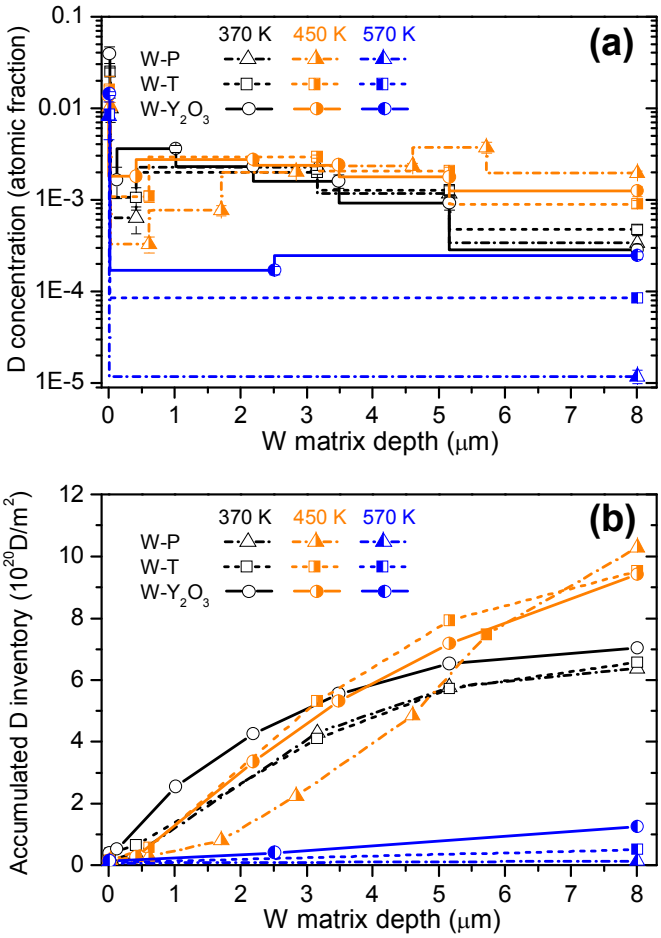

Fig. 8: *(a) D depth profiles (topmost 8 μm) for various tungsten materials exposed at 370, 450 and 570 K determined by NRA. (b) The respective accumulated D inventories versus the depth (integral D amount from the surface to the respective depth calculated from the depth profiles presented in (a)) for these materials.*

For exposure at **370 K**, W−Y_2O_3 shows a second D concentration maximum (3.6×10^{-3}) in the depth ranging from 120 nm to 1 μm. For larger depth the D concentration decreases approximately exponentially to 2.8×10^{-4}. In comparison, both W−P and W−T show a lower second D concentration maximum (about 2.0×10^{-3}) in a depth between 420 nm and 3.2 μm, but maintain a slightly higher D concentration at large depth. However, it has to be stated that the difference of the D concentrations for depths larger than about 5 μm are comparable to the experimental uncertainty. At 370 K the total accumulated D inventory (Fig. 8b) in W−Y_2O_3 is at low depth significantly higher than in W−T and W−P, but towards larger depth (≥ 2 μm) the relative difference decreases and at 8 μm it is comparable to the experimental uncertainty (7.0×10^{20}, 6.5×10^{20} and 6.4×10^{20} D m^{-2} for W−Y_2O_3, W−T and W−P, respectively).

After exposure at **450 K**, both W−T and W−Y_2O_3 show the second D concentration maximum at about 2.7 to 2.9×10^{-3} in the depth range of 0.5 to 3 μm and then decrease to 1×10^{-3}. For W−P, the D concentration increases gradually from 3.4×10^{-4} to 3.7×10^{-3} in the first 5.7 μm and remains at 2.0×10^{-3} for larger depth. Therefore, as shown in Fig. 8b, W−P exposed at 450 K accumulates significantly less D in the first 5.7 μm, but shows a stronger increase towards larger depth such that the total D inventories in the topmost 8 μm are significantly higher than at 370 K. This contrasts the trend reported in [21], but is likely due to

the stronger blistering activity observed here at 450 K. At 370 K, the D depth profile and total D retention found here and in [21] are comparable. The total D inventories for W−P, W−T and W−Y_2O_3 reach 10.3, 9.5 and 9.4×10^{20} D m^{-2}, respectively. The main difference in the depth profiles after loading at 370 and 450 K are that in the region close to the surface up to about 1 μm the D concentration for 450 K is comparable or slightly lower than at 370 K, the second concentration maximum is of comparable magnitude, but shifted to larger depth and the concentration in depths larger than 5 μm is significantly larger for 450 K loading.

The depth profiles become flatter at **570 K**. Also, the bulk concentration typically becomes smaller. As a result, the three W grades show at 570 K a retention that is about one order of magnitude lower than that at 450 K. Moreover, W−Y_2O_3 shows a bulk D concentration of about 2.5×10^{-4}, which is about 2 times higher than in W−T, and 20 times higher than in W−P. The very low D concentration in W-P at high temperatures under these loading conditions is in agreement with the observations reported in [21].

4 Discussion

As illustrated in Figs. 4 and 8, the implantation temperature is an important factor affecting both blistering behavior and the amount of retained D within the topmost 8 μm of the three W grades. Such temperature dependence has also been reported for many different experimental conditions [20,21,[41],[42],[43],[44],[45],[46],[47],[48]]. A basic explanation for the temperature dependence of blistering and deuterium retention in tungsten can be found in [[49],[50]]. It will not be further detailed in the present work.

Apart from the implantation temperature also the tungsten grade significantly influences the blistering behavior, as shown in Fig. 4 (see also [20]). The comparison of the two pure W grades with respect to blistering revealed the importance of the W grain structure. The microstructure of W−P is layered with highly elongated grains arranged parallel to the surface [32,33]. The grain boundaries of these highly elongated grains provide a natural interface for blisters nucleation and large-scale crack propagation near the surface [20], thus resulting in large blisters with a comparatively high height. For W−T, the W grains are less deformed as compared with those of W−P (Fig. 1). In this case, the distance from the surface to the first grain boundary is larger than in W−P. It could be too thick to be bulged up by elastic and plastic deformation, such that no blisters comparable to those in W−P can be formed. Obviously, this leads to the formation of surface structures with much smaller size and height. Considering the similar grain structure in W−T and W−Y_2O_3, we could speculate that the higher amount of surface structures with smaller sizes on the exposed surface of W−Y_2O_3 is correlated with the chemical impurities (such as Y_2O_3 dispersions and WC precipitates) [23,[51],[52],[53],[54],[55],[56]] and residual pores (see Fig. 2), which leads to a higher density of intrinsic trap sites in W−Y_2O_3. The chemical impurities (in particular, Y_2O_3 particles) and residual pores in W−Y_2O_3 might, on the one hand, serve as nucleation points, and, on the other hand, act as a sinks for D suppressing the growth of blisters by trapping the implanted D and preventing its diffusion into the bulk [[57],[58]]. Otherwise, the mechanical properties of the material [[59],[60],[61],[62]], e.g., bond strength of grain boundaries and interfaces, could also be considered as a reason for the less significant surface modification of W−Y_2O_3. But so far not much is known about the bond strength of W grain boundaries or the interface between W and dispersion particles, such that this hypothesis cannot be tested. The conceivable effects of D

implantation into the W matrix and the change of mechanical properties with the implantation temperature increase the complexity even further.

The total amounts of D retained within the NRA information depth for the three different investigated W materials are for each loading temperature (370, 450, and 570 K) well comparable with each other. However, a more detailed inspection reveals differences in the local D concentrations, as shown in Fig. 8a. For example, after exposure at 570 K, W−Y_2O_3 exhibits a D concentration that is 2 times higher than in W−T, and 20 times higher than in W−P. This is interpreted as a higher density of high-energy trap sites in W−Y_2O_3, which consist of originally existing ones and new trap sites created during deuterium plasma exposure. Moreover, it is observed that W−Y_2O_3 exposed at 370 K has much smaller blisters and shows the second D concentration maximum in a shallower depth than the two pure W grades. Furthermore, W−P exposed at 450 K has much larger blisters than W−T and its second D concentration maximum is shifted to larger depth. It has been suggested that the observed blister size is correlated with the depth of the underlying blister cavity, in the sense that the cavity of larger blisters occurs in larger depth [20,[63]]. It has further been suggested before that the position of the second D concentration maximum position seems to be correlated with the depth of the blister cavities [21]. This seems plausible since the blisters are filled with D_2 gas [29], and the formation of blisters can in addition locally increase the trap density by creating dislocations around the deformed material [21,[64]]. The observations described above for 450 K – increasing blister size in the order W−Y_2O_3, W−T, W−P and corresponding shift of the D concentration maximum to larger depth – seem to be in agreement with that proposition.

5 Summary

The blistering and near-surface deuterium retention of Y_2O_3-doped W and two different pure W grades were investigated after D plasma exposure up to a D implantation fluence of 6×10^{24} D m^{-2} at elevated temperatures (370, 450 and 570 K) with a moderate ion flux of about 9×10^{19} D m^{-2} s^{-1} and an ion energy of 38 eV/D. The implantation temperature played a significant role in the blistering behavior and the amount of retained D, which is consistent with previous investigations [20,21,41,42,43,44,45,46,47,48]. Exposure at 370 K led to the appearance of a large number of small blisters. After exposure at 450 K, the blister density is somewhat lower, but the blisters are in average larger and higher, and the total inventory is much higher as compared to the exposure at 370 K. After exposure at 570 K no blister was detected on any of the samples and the total D inventory is about one order of magnitude lower than at 450 K. The W grade also strongly influenced the blistering. For example, at the implantation temperature of 450 K, W−P showed spherical blisters with an average diameter of 32 μm and a height ranging from 300 nm to 2.2 μm, while W−T exhibited plateau-like blisters with smaller sizes (average diameter: 8.8 μm, height distribution range: 0.2−1 μm). For W−Y_2O_3, the sizes of the blisters were further reduced (average size: 2.6 μm, height range: 0.2−0.8 μm). In comparison, however, the effect of specimen type on near-surface deuterium retention was much less obvious. For the three W specimens exposed at each temperature, the depth profiles were slightly different and the total D inventories were quite comparable. However, a more detailed inspection reveals differences in the local D concentrations. For example, after exposure at 570 K, W−Y_2O_3 exhibits a D concentration that is 2 times higher

than in W−T, and 20 times higher than in W−P.

Overall, under the present exposure condition, W−Y_2O_3 suffered less surface modifications and did not exhibit much higher retention as compared to the two different pure W grades.

Acknowledgements

The stay of Mingyue Zhao at IPP was made possible through the financial support of the Chinese Scholarship Council which is gratefully acknowledged. We would further like to thank Thomas Dürbeck and Stefan Kapser for the help with sample preparation, Gabriele Matern and Stefan Elgeti for the help with the SEM investigations and Klaus Schmid and Matej Mayer for the help with evaluation of the ion beam measurements.

References

1 R. Aymar. ITER status, design and material objectives. J. Nucl. Mater. 307–311 (2002) 1–9.

2 R. Neu, V. Bobkov, R. Dux, A. Kallenbach, Th. Pütterich, H. Greuner, O. Gruber, A. Herrmann, Ch. Hopf, K. Krieger, C.F. Maggi, H. Maier, M. Mayer, V. Rohde, K. Schmid and W. Suttrop. Final steps to an all tungsten divertor tokamak. J. Nucl. Mater. 363–365 (2007) 52–59.

3 V. Barabash, A. Peacock, S. Fabritsiev, G. Kalinin, S. Zinkle, A. Rowcliffe, J.-W. Rensman, A.A. Tavassoli, P. Marmy, P.J. Karditsas, F. Gillemot and M. Akiba. Materials challenges for ITER–Current status and future activities. J. Nucl. Mater.367–370 (2007) 21–32.

4 M.R. Gilbert, J.–Ch. Sublet. Neutron–induced transmutation effects in W and W-alloys in a fusion environment. Nucl. Fusion 51 (2011) 043005.

5 X. Liu, J.M. Chen, Y.Y. Lian, J.H. Wu, Z.Y. Xu, N.M. Zhang, Q.M. Wang, X.R. Duan, Z.H. Wang and J.M. Zhong. Vaccum hot-pressed beryllium and TiC dispersion strengthened tungsten alloy developments for ITER and future fusion reactors. J. Nucl. Mater. 442 (2013) S309–S312.

6 L.M. Luo, X.Y. Tan, H.Y. Chen, G.–N. Luo, X.Y. Zhu, J.G. Cheng and Y.C. Wu. Preparation and characteristics of W–1 wt.% TiC alloy via a novel chemical method and spark plasma sintering. Powder Technol. 273 (2015) 8–12.

7 J. Riesch, J.–Y. Buffiere, T. Höschen, M. Di Michiel, Ch. Linsmeier and J.–H. You. In situ synchrotron tomography estimation of toughening effect by semi-ductile fibre reinforcement in a tungsten-fibre-reinforced tungsten composite system. Acta Mater. 61 (2013) 7060–7071.

8 H. Kurishita, Y. Amano, S. Kobayashi, K. Nakai, H. Arakawa, Y. Hiraoka, T. Takida, K. Takebe and H. Matsui, Development of ultra-fine grained W–TiC and their mechanical properties for fusion applications. J. Nucl. Mater. 367–370, (2007) 1453–1457.

9 H. Kurishita, S. Matsuo, H. Arakawa, S. Kobayashi, K. Nakai, T. Takida, K. Takebe and M. Kawai, Superplastic deformation in W–0.5wt.% TiC with approximately 0.1μm grain size. Mater. Sci. Eng. A 477 (2008) 162–167.

10 H. Kurishita, S. Matsuo, H. Arakawa, M. Narui, M. Yamazaki, T. Sakamoto, S. Kobayashi, K. Nakai, T. Takida, K. Takebe, M. Kawai and N. Yoshida. High temperature tensile properties and their application to toughness enhancement in ultra-fine grained W-(0-1.5)wt% TiC. J. Nucl. Mater. 386–388 (2009) 579-582.

11 H. Kurishita, S. Matsuo, H. Arakawa, T. Sakamoto, S. Kobayashi, K. Nakai, T. Takida, M. Kato, M. Kawai and N. Yoshida. Development of re-crystallized W–1.1%TiC with enhanced room-temperature ductility and radiation performance. J. Nucl. Mater. 398 (2010) 87–92.

12 M. Battabyal, R. Schäublin, P. Spätig and N. Baluc. W–2 wt.% Y_2O_3 composite: Microstructure and mechanical properties. Mater. Sci. Eng. A 538 (2012) 53–57.

13 M. Battabyal, R. Schäublin, P. Spätig, M. Walter, M. Rieth and N. Baluc. Microstructure and mechanical properties of a W–2wt.% Y_2O_3 composite produced by sintering and hot forging. J. Nucl. Mater. 442 (2013) S225-S228.

14 M. Zhao, Z. Zhou, M. Zhong, J. Tan, Y. Lian and X. Liu, Thermal shock behavior of fine grained W– Y_2O_3 materials fabricated via two different manufacturing technologies, J. Nucl. Mater. 470 (2016) 236–243.

15 M. Mabuchi, K. Okamoto, N. Saito, T. Asahina and T. Igarashi. Deformation behavior and strengthening mechanisms at intermediate temperatures in W–La_2O_3. Mater. Sci. Eng. A. 237 (1997) 241–249.

16 I. Wesemann, W. Spielmann, P. Heeland A. Hoffmann. Fracture strength and microstructure of ODS tungsten

alloys. Int. J. Refract. Met. Hard Mater. 28 (2010) 687–691.

17 W.M. Shu, G.–N. Luo and T. Yamanishi. Mechanisms of retention and blistering in near-surface region of tungsten exposed to high flux deuterium plasmas of tens of eV, J Nucl. Mater. 367–370, Part B (2007) 1463–1467.

18 J.B. Condon and T.J. Schober. Hydrogen bubbles in metals. J. Nucl. Mater. 207 (1993) 1–24.

19 C.H. Skinner, A.A. Haasz, V.K. Alimov, N. Bekris and R.A. Causey. Recent Advances on Hydrogen Retention in ITER's Plasma-Facing Materials: Beryllium, Carbon, and Tungsten. Fusion Sci. Technol. 54 (2008) 891–945.

20 M. Balden, A. Manhard and S. Elgeti. Deuterium retention and morphological modifications of the surface in five grades of tungsten after deuterium plasma exposure. J. Nucl. Mater. 452 (2014) 248–256.

21 A. Manhard, 2010 Deuterium Inventory in Tungsten after Plasma Exposure: A. Microstructural Survey (Ph.D. Thesis, University Augsburg), Technical Report IPP 17/34, Garching 2012, Web link: http://hdl.handle.net/11858/00-001M-0000-0026-E65B-C

22 M. Zibrov, M. Mayer, E. Markina, K. Sugiyama, M. Betzenbichler, H. Kurishita, Y. Gasparyan, O.V. Ogorodnikova, A. Manhard and A. Pisarev. Deuterium retention in TiC and TaC doped tungsten under low-energy ion irradiation, Phys. Scr. 2014 (2014) 14050.

23 M. Zibrov, M. Mayer, L. Gao, S. Elgeti, H. Kurishita, Y. Gasparyan and A. Pisarev, Deuterium retention in TiC and TaC doped tungsten at high temperatures. J. Nucl. Mater. 463 (2015) 1045–1048.

24 Y. Ueda, T. Funabiki, T. Shimada, K. Fukumoto, H. Kurishita and M. Nishikawa. Hydrogen blister formation and cracking behavior for various tungsten materials. J Nucl. Mater. 337–339 (2005) 1010–1014.

25 M. Zhao, Z. Zhou, M. Zhong and J. Tan. Effect of hot rolling on the microstructure and fracture behavior of a bulk fine-grained W–Y_2O_3 alloy. Mater. Sci. Eng. A. 646 (2015) 19–24.

26 O.V. Ogorodnikova, J. Roth and M. Mayer, Pre-implantation and pre-annealing effects on deuterium retention in tungsten. J. Nucl. Mater. 373 (2008) 254–258.

27 A. Manhard, U. von Touissant, T. Dürbeck, K. Schmid and W. Jacob. Statistical Analysis of Blister Bursts during Temperature Programmed Desorption of Deuterium-implanted Polycrystalline Tungsten. Physica Scripta T145, (2011) 014038.

28 A. Manhard, K. Schmid, M. Balden and W. Jacob. Influence of the microstructure on the deuterium retention in tungsten, J. Nucl. Mater. 415 (2011) S632–S635.

29 M. Balden, S. Lindig, A. Manhard, and J.H. You. D_2 gas-filled blisters on deuterium-bombarded tungsten. J. Nucl. Mater. 414 (2011) 69–72.

30 X. Zhang, Q. Yan, S. Lang, M. Xia and C. Ge. Texture evolution and basic thermal–mechanical properties of pure tungsten under various rolling reductions. J. Nucl. Mater. 468 (2016) 339–347.

31 Y. Huang, Y. Liu, Q. Li, X. Liu and C. Yang. Relevance between microstructure and texture during cold rolling of A3104 aluminum alloy. J. Alloys Comp. 673(2016) 383–389.

32 A. Manhard, M. Balden and S. Elgeti, Quantitative microstructure and defect density analysis of polycrystalline tungsten reference samples after different heat treatments. Practical Metallogr. 52 (2015) 437–466.

33 A. Manhard, G. Matern and M. Balden. A step-by-step analysis of the polishing process for tungsten specimens. Practical Metallogr. 50 (2013) 5–16.

34 A. Manhard, T. Schwarz–Selinger and W. Jacob. Quantification of the deuterium ion fluxes from a plasma source, Plasma Sources Science and Technology 20 (2011) 015010.

35 V.Kh. Alimov, M. Mayer and J. Roth. Differential cross section of the D (^{3}He,p) ^{4}He nuclear reaction and depth profiling of deuterium up to large depths. Nucl. Instr. and Meth. B 234 (2005) 169–175.

36 K. Schmid and U. von Toussaint. Statistically sound evaluation of trace element depth profiles by ion beam analysis. Nucl. Instr. Meth. B 281 (2012) 64–71.

37 S. Bielesch, M. Oberkofler, H.–W. Becker, H. Maier, D. Rogalla, T. Schwarz Selinger and C. Linsmeier. Experimental resolution of deuterium and hydrogen depth profiling with the nuclear reactions D (^{3}He, p) α and p (^{15}N, α, γ) ^{12}C. Nucl. Instrum. Meth. Phys. Res. B 317 (2013) 121–125.

38 R. B. Bergmann and A. Bill. On the origin of logarithmic-normal distributions: An analytical derivation, and its application to nucleation and growth processes. J. Cryst. Growth 310 (2008) 3135.

39 A.V. Teran, R.B. Bergmann and A. Bill. Time-evolution of grain size distributions in random nucleation and growth crystallization processes. Phys. Rev. B 81 (2010) 075319.

40 L. Gao, W. Jacob, U. von Toussaint, A. Manhard, M. Balden, K. Schmid and T. Schwarz-Selinger. Deuterium supersaturation in low-energy plasma-loaded tungsten surfaces. Nucl. Fusion 57, 016026 (11pp) (2017).

41 S Lindig, M Balden, V Kh Alimov, T Yamanishi, W M Shu and J Roth. Subsurface morphology changes due to deuterium bombardment of tungsten. Phys. Scr. T138 (2009) 14040.

42 T. Shimada, Y. Ueda and M. Nishikawa. Mechanism of blister formation on tungsten surface. Fusion Eng. Des. 66–68 (2003) 247–251

43 G.–N. Luo, W.M.Shu, H. Nakamura, S. O'Hira and M. Nishi. Ion species control in high flux deuterium plasma beams produced by a linear plasma generator. Rev. Sci. Instrum. 75 (2004) 4374.

44 M.H.J. 't Hoen, M. Mayer, M. Balden, S. Lindig, A. Manhard, A.W. Kleyna and P.A. Zeijlmans van Emmichoven. High flux and fluence exposures of pre-irradiated tungsten to deuterium plasmas, in: Proc. 14th Intern. Workshop on Plasma Facing Materials and Components for Fusion Application, Jülich, Germany, May 13–17, 2013.

45 V.K. Alimov, W.M. Shu, J. Roth, K. Sugiyama, S. Lindig, M. Balden, K. Isobe and T. Yamanishi. Surface morphology and deuterium retention in tungsten exposed to low-energy, high flux pure and helium seeded deuterium plasmas, Phys. Scr. T138 (2009) 014048.

46 W.M. Shu, E. Wakai and T. Yamanishi. Blister bursting and deuterium bursting release from tungsten exposed to high fluences of high flux and low energy deuterium plasma. Nucl. Fusion 47 (2007) 201–209.

47 V.K. Alimov, B. Tyburska–Püschel, S. Lindig, Y. Hatano, M. Balden, J. Roth, K. Isobe, M. Matsuyama and T. Yamanishi. Temperature dependence of surface morphology and deuterium retention in polycrystalline ITER-grade tungsten exposed to low-energy, high-flux D plasma. J. Nucl. Mater. 420 (2012) 519–524.

48 V.K. Alimov, W.M. Shu, J. Roth, S. Lindig, M. Balden, K. Isobe and T. Yamanishi. Temperature dependence of surface topography and deuterium retention in tungsten exposed to low-energy, high-flux D plasma. J. Nucl. Mater. 417 (2011) 572–575.

49 G. –N. Luo, W.M. Shu and M. Nishi. Influence of blistering on deuterium retention in tungsten irradiated by high flux deuterium 10-100 eV plasmas. Fusion Eng. Des. 81(2006) 957–962.

50 W.M. Shu, K. Isobe, and T. Yamanishi. Temperature dependence of blistering and deuterium retention in tungsten exposed to high-flux and low-energy deuterium plasma. Fusion Eng. Des. 83(2008) 1044–1048.

51 N. Enomoto, S. Muto, T. Tanabe, J.W. Davis and A.A. Haasz. Grazing-incidence electron microscopy of surface blisters in single- and polycrystalline tungsten formed by H^+, D^+ and He^+ irradiation. J. Nucl. Mater. 385 (2009) 606–614.

52 K. Heinola and T. Ahlgren. Hydrogen retention to impurities in tungsten: A multi-scale study. J. Nucl. Mater. 438, Supplement (2013) S1001–S1004.

53 S.M. Lee and J.Y. Lee. The effect of the interface character of TiC particles on hydrogen trapping in steel. Acta Metall. 35 (1987) 2695–2700.

54 H.G. Lee and J.Y. Lee. Hydrogen trapping by TiC Particles in iron. Acta metall. 32 (1984) 131–136.

55 J. Takahashi, K. Kawakami, Y. Kobayashi, and T. Tarui. The first direct observation of hydrogen trapping sites in TiC precipitation-hardening steel through atom probe tomograph. Scripta Mater. 63 (2010) 261–264.

56 J. L. Lee and J. Y. Lee. The interaction of hydrogen with the interface of Al_2O_3 particles in iron. Metall. Trans. A. 17 (1986) 2183–2186.

57 L. Gao, U. von Toussaint, W. Jacob, M. Balden and A. Manhard. Suppression of hydrogen-induced blistering of tungsten by pre–irradiation at low temperature. Nucl. Fusion. 54 (2014) 122003.

58 J.P. Roszell, A.J. Labelle, P. Brodersen, J.W. Davis and A.A. Haasz. D retention in C- and O-contaminated tungsten during D+ irradiation. J. Nucl. Mater. 427 (2012) 193–199.

59 Y. Liang and P. Sofronis. Toward a phenomenological description of hydrogen-induced decohesion at particle/matrix interfaces, J Mech. Phys. Solids. 51 (2003) 1509–1531.

60 J.P. Hirth. Effects of hydrogen on the properties of iron and steel. Metall. Trans. 11A (1980) 861–890.

61 F.G. Wei and K. Tsuzaki. Hydrogen absorption of incoherent TiC particles in iron from environment at high temperatures. Metall. Mater. Trans. A. 35A (2004) 3155–3163.

62 R. Valentini, A. Solina, S. Matera and P. De Gregorio. Influence of Titanium and Carbon Contents on the Hydrogen Trapping of Microalloyed Steels. Metall. Mater. Trans. A. 27A (1996) 3773.

63 Y. Ueda, T. Funabiki, T. Shimada, K. Fukumoto, H. Kurishita and M. Nishikawa. Hydrogen blister formation and cracking behavior for various tungsten materials. J. Nucl. Mater. 337–339 (2005) 1010–1014.

64 A. Manhard, U. von Toussaint, M. Balden, S. Elgeti, T. Schwarz-Selinger, L. Gao, S. Kapser, T. Płociński, J. Grzonka, M. Gloc and Ł. Ciupiński. Microstructure and defect analysis in the vicinity of blisters in polycrystalline tungsten. Nucl. Mater. Energy, in the press, doi: 10.1016/j.nme.2016.10.014